PHYSICAL REVIEW C VOLUME 51, NUMBER 4 APRIL 1995

Total cross section measurements of $^{16}O+^{232}Th$ incomplete fusion followed by fission at 140 MeV

E. P. Gavathas, A. D. Frawley, R. C. Kline, and L. C. Dennis
Department of Physics, Florida State University, Tallahassee, Florida 32306

(Received 8 February 1994; revised manuscript received 29 November 1994)

Total cross sections for incomplete fusion followed by fission have been measured for the reaction $^{16}O+^{232}Th$ at 140 MeV. In-plane and out-of-plane measurements were made of cross sections for beamlike fragments in coincidence with fission fragments. The beamlike fragments were detected with a Bragg curve spectrometer which is position sensitive in the polar direction. The beamlike particles observed in coincidence with fission fragments were He, Li, Be, B, C, N, and O. One fission fragment from each reaction was detected by one of three surface barrier detectors using time of flight for particle identification. The measured cross section due to fission following incomplete fusion is 747±112 mb, or 42% of the total fission cross section. The strongest incomplete fusion channels were the He and C channels. The average transferred angular momentum for each incomplete fusion channel was predicted using the $Q_{\rm opt}$ model of Wilczyński so that the K distribution could be estimated from the rotating liquid drop model. The experimental angular distributions were fitted using the saddle-point transition state model, with the transferred angular momentum J and the dealignment factor α_0 as free parameters. The saddle-point transition state model is found to adequately describe the observed angular correlations for fission following incomplete fusion. The fitted parameter J showed systematic deviations from the $Q_{\rm opt}$ model predictions, suggesting that the average impact parameter is larger than expected for heavy projectile fragments.

PACS number(s): 25.70.Jj, 25.70.Hi

I. INTRODUCTION

Heavy ion induced nuclear fission has been studied extensively (see for example, R. Vandenbosch *et al.* [1], P. David *et al.* [2], W. Schröder *et al.* [3], L. C. Vaz *et al.* [4], R. Freifelder *et al.* [5]), and the saddle-point transition state model (STSM) [6] has been successful in predicting fission fragment angular distributions for systems which are not extremely fissile. Back *et al.* in 1981 [7] reported fission fragment angular distributions from reactions of ^{32}S on ^{197}Au, ^{232}Th, ^{238}U, and ^{248}Cm targets and, in some cases, the anisotropy of the observed angular distributions was smaller than anticipated from STSM calculations. It was argued by several authors [8–12] that, for vanishing fission barriers, only partial equilibration of the compound nucleus occurs prior to fission, therefore the K distribution at the saddle point cannot be predicted by equilibrium compound nucleus models. On the other hand, Bond [13,14] and Rossner [15,16] put forward models in which it is assumed that an equilibrated compound nucleus is found, but that the K distribution is not frozen at the saddle point but keeps evolving until the scission point is reached.

In the analyses of fission fragment angular distributions discussed above, it has been assumed that incomplete fusion contributions were negligible, or they have been estimated using models which are of questionable reliability for this purpose. There is very little data for fission following incomplete fusion, and no measurements of total cross sections. Therefore the role of incomplete fusion in determining fission fragment angular distributions is so far rather poorly understood. In order to study the importance of incomplete fusion in determining fission cross sections, we have measured cross sections for incomplete fusion followed by fission for the reaction of 140 MeV ^{16}O with ^{232}Th. The major goals were to measure the total fission cross sections corresponding to the incomplete fusion channels, to study the fission fragment angular correlations, and to compare them with existing models. The $^{16}O+^{232}Th$ reaction at 140 MeV was chosen because inclusive data are available [17], and because this reaction was studied by Bond [14] in some detail. Transfer induced fission has been studied for this reaction at energies near the Coulomb barrier by Lestone *et al.* [18], who measured integrated cross sections, and by Videbaek *et al.* [19].

For the transformation of the cross sections from the laboratory frame to the frame of reference of the recoiling fissioning nucleus, Wilczyński's $Q_{\rm opt}$ model [20] was used to estimate the excitation energy of the fissioning nucleus, needed to calculate the necessary kinematic quantities. Viola systematics [21] were used to estimate the kinetic energy of the fission fragments assuming symmetric fission.

II. EXPERIMENT

A. Experimental setup

The 140 MeV ^{16}O beam from the Florida State University superconducting linear accelerator bombarded a ThF_4 target whose thickness was 370 $\mu g/cm^2$. The target was evaporated on a 50 $\mu g/cm^2$ C foil. Fission frag-

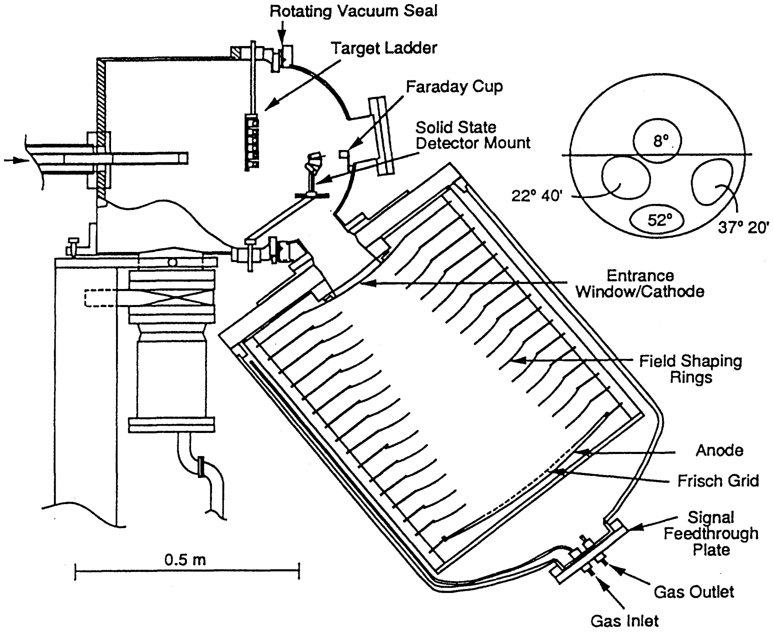

FIG. 1. Experimental apparatus.

ments were detected with three surface barrier detectors. The beamlike fragments observed, ranging from He to O, were detected with a Bragg curve spectrometer. Signals produced by H are below the noise threshold of the Bragg curve spectrometer, therefore the H cross sections were not observed. The scattering chamber and Bragg curve spectrometer are shown schematically in Fig. 1. Not shown is a movable slit which was used to calibrate the position signal from the Bragg curve spectrometer. The down-beam side of the scattering chamber consists of a hemispherical cap supporting four slightly overlapping ports. The Bragg curve spectrometer can be mounted on any port, allowing it to detect scattered particles emitted at angles of up to 60.5° with respect to the beam axis. The cap, mounted on a sliding O-ring seal, can be rotated by 2π about the beam axis. The rotating seal apparatus is mounted on the scattering chamber via a G10 fiberglass ring, which electrically isolates the detectors and electronics from the beam line. Only the second, third, and fourth ports were used for this experiment. The range of θ_{BCS} covered was 14.2° to 60.5°.

Two arms, located at the top and bottom of the scattering chamber, supported the Bragg curve spectrometer position calibration slit and the fission detector array, respectively. These supporting arms are able to rotate about the target position. A desired fission fragment detector angle or Bragg curve spectrometer position calibration slit angle could be set within two tenths of a degree. This accuracy was determined by comparing results of low energy elastic scattering measurements with Rutherford scattering calculations of the angular distribution.

The beam energy, energy spread, and the product of the target thickness and beam current were monitored during the experiment using a silicon surface barrier detector. The monitor detector was mounted on the hemispherical cap near the Faraday cup, at approximately 15.6° from the beam axis. A tantalum collimator limited the solid angle of the monitor detector to 0.43 msr.

The fission fragments were detected by an array of three identical silicon surface barrier detectors and were identified by measuring the time of flight relative to the pulsed beam from the linac. The detectors were 30° apart at a distance of 10 cm from the target. The detectors in this array were able to cover polar angles between 10° and 170° in the horizontal plane. Figure 2 shows the fission fragment detector geometry. The thickness of the fission fragment detectors was 300 μm, sufficient to stop all particles of interest including elastically scattered ^{16}O, and the total active area was 150 mm^2. Circular tantalum collimators placed just in front of the detectors limited the solid angles to 14.5 msr for the second and third detectors. For measurements at angles $> 10°$, the solid angle was set at 9.7 msr for the first detector. For measurements at 10°, where the count rates are considerably

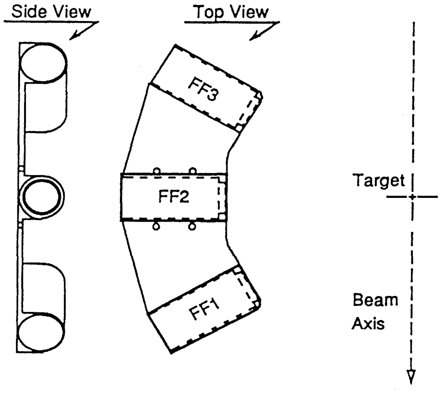

FIG. 2. Fission fragment detector array.

higher, the first fission fragment detector had its solid angle reduced to 2.4 msr. In addition to the tantanlum mask, which defined the detector solid angle, a cylindrical collimator placed in front of each fission fragment detector served as a shield from possible stray particles scattered by the beam line collimation system and the target holder, and also as a support for a pair of ceramic magnets which were placed on the top and the bottom of each of the cylindrical collimators. The magnet pairs created a magnetic field of a few thousand Gauss, which suppressed δ electrons from the target. Without the magnets, δ electrons caused the fission fragment detectors to be very noisy.

The Bragg curve spectrometer [22] is a gas ionization chamber having large acceptance and high stopping power. It provides complete Z identification for ions heavier than H, and for particle energies above approximately 1.75 MeV per nucleon, but it does not provide mass identification. The detector gas is P-10 and the active detector depth is 60 cm. The anode, the Frisch grid, the field shaping rings, and the entrance window are spherical segments with their centers located at the target. The voltages of the 14 field shaping rings are set by a resistive chain to produce a radial electron collection field, so that all electrons from a given incident particle are collected at a point on the anode. In order to prevent the incoming electrons from inducing a charge on the anode until they are close to it, a grounded Frisch grid is placed 0.75 cm in front of the anode. The 7.6 μm thick aluminized Kapton entrance window is supported by a stainless steel mesh of wire thickness 0.0045 inches and mesh size 0.1 by 0.1 inches, resting on aluminum vanes which prevent the window from collapsing as a result of the up to 2.5 atm pressure difference between the Bragg curve spectrometer gas volume and the scattering chamber. For the operating pressure used here of 2 atm, the entrance window is at -20 KV, with the Frisch grid at ground potential. At 2.0 atm the detector stops α particles of up to 44 MeV, and heavier ions at all energies of interest in this experiment.

A mask 17° long in the polar (θ_{BCS}) direction by 4.9° wide was installed in front of the Bragg curve spectrometer entrance window, hence the Bragg curve spectrometer solid angle was 25 msr. The entrance window of the detector is located 39 cm from the target. The anode is a rectangular strip of resistive C evaporated onto a fiberglass spherical segment. The C strip has 1.1 KΩ resistance along the θ_{BCS} direction. The charge collected at each end of the strip is measured to obtain the position and hence the θ_{BCS} value. The resolution of the θ_{BCS} measurement varies from 0.5° to 1.5° depending on the location on the resistive strip. A 666 volt potential was used between the Frisch grid and the anode.

The time dependence of the signal detected by the Bragg curve spectrometer reflects the shape of the Bragg curve. The maximum height is characteristic of the Z of the detected particle, the width is a measure of the range, and the area under the Bragg curve is proportional to the energy.

The position information obtained from resistive charge division in the Bragg curve spectrometer anode was used to divide the Bragg curve spectrometer anode into seven angle bins, each bin being 2.4° wide. The bin boundaries were determined with the Bragg curve spectrometer on port 2 by placing a 1.5 mm wide vertical slit in front of the Bragg curve spectrometer at angles corresponding to the six bin boundaries and recording the position spectrum resulting from 140 MeV ^{16}O reactions on a Au target. The charge collected from the forward end of the Bragg curve spectrometer anode divided by the sum of the charge collected from both ends of the anode defines the position. The position peak centroids that resulted from the above measurements were used as the position bin boundaries.

During off-line analysis, the bin boundaries were determined independently for each Z detected in the Bragg curve spectrometer in order to determine whether the bin boundaries were dependent on the detected particle Z, and it was concluded that the position bin boundaries were independent of the detected particle Z.

The purpose of this experiment is to detect beamlike particles in the Bragg curve spectrometer in coincidence with fission fragments in the fission fragment detectors. However, the fission fragment detectors and the Bragg curve spectrometer all detect fission fragments, beamlike particles, and recoiling residues from reactions with C and F in the ThF_4 target. Therefore there are many true coincidences between the Bragg curve spectrometer and the fission fragment detectors which are of no interest in the present experiment. This large number of uninteresting true coincidences could be rejected only by having good particle identification, particularly of the fission fragments. In order to establish coincidences with fission fragments, a set of gates was drawn around the fission fragment group in the fission fragment detector energy versus time-of-flight spectra. An example is shown in Fig. 3.

During the coincidence measurements, a BCS count rate of approximately 5000 counts per second was maintained in order to control the number of rejected events due to pileup in the detector electronics. At 5000 counts per second, the rejection rate was approximately 12%. A detailed discussion of the electronics is presented in [22]. A LeCroy model 2262 waveform digitizer was used to record the signals from the Bragg curve spectrometer, sampling them into 316 channels. In software analysis of the digitized signals, the Bragg peak height was determined by integration of the area under a narrow window around the peak of the pulse, and the range of the particle was determined from the length of the pulse. The position was determined by the ratio of the total area under the Bragg curve spectrometer position signal and the total area under the summed Bragg curve spectrometer signal. With the exception of the Bragg curve spectrometer signals, all other signals, such as the fission fragment detector energy signals, were processed by peak sensing ADC's.

In order to establish a coincidence event, the following scheme was employed. When one of the fission fragment detectors fired, a TAC window was opened. The TAC was stopped by the occurrence of a Bragg curve spectrometer event or after 14.9 μs. If a Bragg curve spectrometer signal occurred within the TAC window, a strobe signal was produced, and the event was recorded as a coincidence event.

The product of the target thickness and the detector solid angle was determined by comparing the yields of low energy 68 MeV ^{16}O ions elastically scattered into the first fission fragment detector from the target with the predictions of the Rutherford scattering cross section formula. The relative solid angles of the other two fission fragment detectors were measured by setting all three detectors at the same laboratory angle and recording elastic scattering yields relative to the fixed monitor detector. The relative solid angle of the Bragg curve spectrometer was estimated from the physical dimensions of the Bragg curve spectrometer mask and the collimator in front of the first fission fragment detector.

III. MEASUREMENTS

Inclusive fission fragment yields were measured from 10° to 170° in steps of 10° using the fission fragment detector array. These measurements were made for comparison with the angular distribution and the total cross section previously reported by Back *et al.* [17]. Only one of the fission fragments was detected.

Coincidence cross sections were measured at 75 combinations of Bragg curve spectrometer angle and fission fragment detector wedge angle. The angles at which the Bragg curve spectrometer was positioned for the coincidence measurements are shown in Table I. The $\phi_{\mathrm{BCS}} = 0^\circ$ direction is beam left, and the $\phi_{\mathrm{BCS}} = 90^\circ$ direction is vertically up in the laboratory frame, i.e., perpendicular to the plane of rotation of the fission fragment detectors. The value of θ_{BCS} in Table I corresponds to the center of the Bragg curve spectrometer, which subtends $\pm 8.5^\circ$ in θ_{BCS}. The fission fragment detector polar angles were varied from 10° to at least 90° in steps of 10° for each setting of θ_{BCS} and ϕ_{BCS}.

TABLE I. Bragg curve spectrometer angle settings.

Port No.	θ_{BCS}	ϕ_{BCS}
2	22.7°	$0^\circ, 45^\circ, 90^\circ, 135^\circ, 225^\circ$
3	37.3°	$0^\circ, 22.5^\circ, 45^\circ, 67.5^\circ, 90^\circ$ $112.5^\circ, 135^\circ, 157.5^\circ, 202.5^\circ$
4	52.0°	$0^\circ, 22.5^\circ, 45^\circ, 67.5^\circ, 90^\circ$ $112.5^\circ, 135^\circ, 157.5^\circ, 202.5^\circ$

As will be discussed in Sec. IV, after conversion to the recoiling fissioning nucleus center-of-mass reference frame, symmetry about $\theta = 90^\circ$ and $\phi = 0^\circ$ and 90° was invoked. Assuming that these symmetries hold, it would have been redundant to measure data with the Bragg curve spectrometer below the plane of the fission fragment detectors, or with the fission fragment detectors backward of about 90° in the lab. Some measurements were made with the Bragg curve spectrometer below the plane of the fission fragment detectors and with the fission fragment detectors behind 90°, to verify that the assumed symmetries were observed. The results are discussed in Sec. IV.

There were no data taken at $\phi_{\mathrm{BCS}} = 180^\circ$ because in this configuration when the fission fragment detector wedge was set at forward angles it blocked the Bragg curve spectrometer mask. The ϕ_{BCS} step size for port 2 was twice that for ports 3 and 4 because of the large coverage of ϕ_{BCS} at each Bragg curve spectrometer angle setting on port 2 relative to ports 3 and 4.

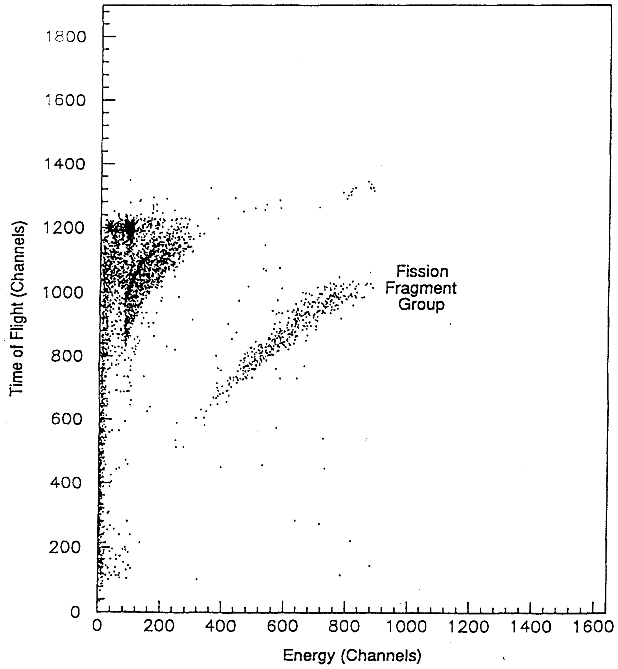

FIG. 3. Typical fission fragment time of flight versus energy spectrum. The location of the fission fragment group makes it easily identifiable. Time of flight decreases with increasing channel number.

IV. DATA REDUCTION

The inclusive fission fragment yields were obtained by gating on the fission fragment group in the inclusive fission fragment energy versus time spectra (Fig. 3). The fission fragment yields were then converted to different cross sections in the laboratory frame of reference, and are shown in Fig. 4.

In order to compare our results with those of a previous experiment [17], the differential cross sections in the laboratory frame were converted to the fissioning nucleus center-of-mass system, assuming complete fusion followed by fission. The results are shown in Fig. 5. Viola systematics [21] were used to estimate the kinetic energy of the fission fragments from the mass and charge of the compound nucleus, assuming symmetric fission. Note that the results of the present experiment show clearly that the assumption of complete fusion is not valid.

The digitized Bragg curve spectrometer signals were analyzed to obtain the Bragg peak height, the energy, the range, and the position of each event. The digitized

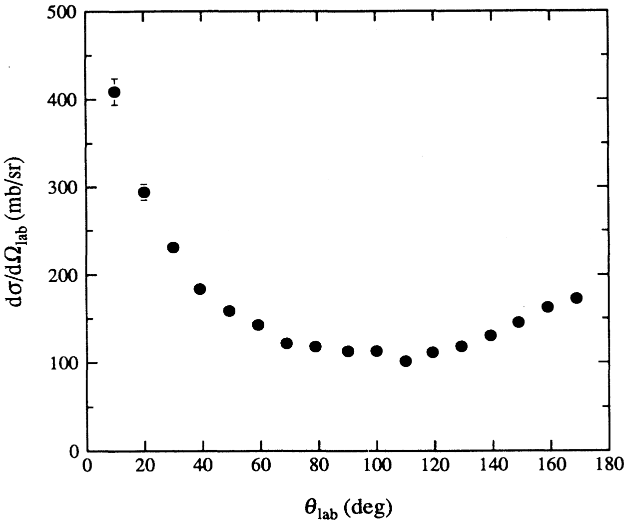

FIG. 4. Inclusive differential cross sections in the laboratory frame for ^{16}O+^{232}Th leading to fission.

signals were examined for evidence of pulse pileup by looking for multiple leading edges. When evidence of pulse pileup was observed the event was rejected, and statistics were kept to allow the yields to be corrected for the losses due to pileup.

The range of the particle detected in the Bragg curve spectrometer is related to the time length of the pulse. The time at which the first electrons reach the anode is complementary to the time length of the pulse. The sum of the two always equals 11.2 μs, the time required for an electron to drift from the entrance window to the anode.

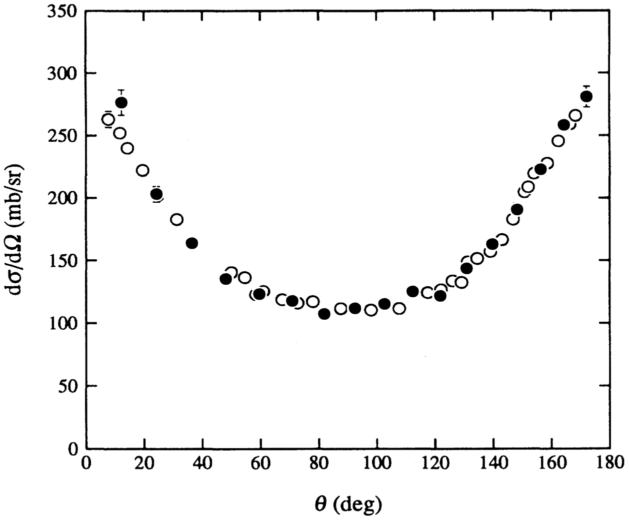

FIG. 5. Inclusive differential cross sections from this work (filled circles) for ^{16}O+^{232}Th leading to fission, after transformation to the rest frame of the recoiling fissioning nucleus by (incorrectly) assuming complete fusion followed by symmetric fission. Data from Ref. [17] have been renormalized to yield a total cross section of 1790 mb and are shown (open circles) for comparison.

Figure 6 shows an example of a two-dimensional scatter plot of the range (the length of the digitized pulse) versus the range TAC signal (the difference in time between the signal from the fission fragment detector and that from the Bragg curve spectrometer). Events along the diagonal line fulfill the complementary relationship between the two signals; therefore, they represent true coincidences. The accidental coincidences are uniformly distributed in the range TAC direction. True coincidences were selected by drawing a gate around the true coincidence locus and accidental coincidence yields were sampled using a second gate which did not include the true coincidence locus. A spectrum of the Bragg peak height versus energy in coincidence with fission fragments is shown in Fig. 7. All of the ejectiles are easily identifiable, with energies which are considerably higher than the particle identification threshold. We did not observe any incomplete fusion products heavier than O.

The number of events in the background gate was subtracted from the number of events in the true coincidence gate, and the net yields were calculated for each Bragg curve spectrometer position bin, for each beamlike ejectile in coincidence with a fission fragment. The net yields were converted to double differential cross sections in the laboratory frame.

Figure 8 shows energy spectra for each ejectile in coincidence with fission fragments, summed over all runs with $\phi_{BCS} = 0^\circ$ on ports 2–4, and for all θ_{FF} angles between 0° and 90°. The most intense channels are He and C. The high energy end of the He spectrum is truncated because the range of He ions exceeds the detector depth for α particles above 44 MeV. The loss of He yield was estimated for each port by drawing a smooth curve through the spectrum and reconstructing its missing part. Since

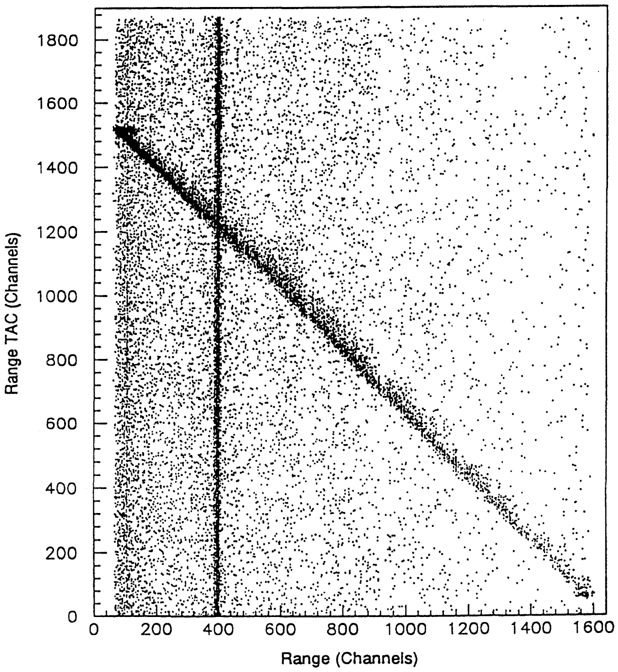

FIG. 6. Range versus range TAC spectrum used to separate true and accidental coincidence events.

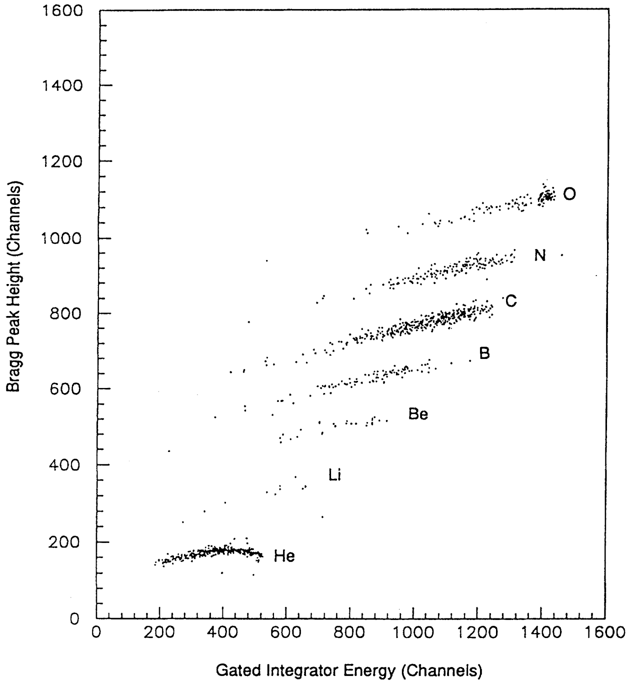

FIG. 7. Two-dimensional scatter plot showing Bragg peak height versus energy for Bragg curve spectrometer events in coincidence with fission fragments. The data were summed over ports 2, 3, and 4, with $\phi_{\mathrm{BCS}} = 0°$ and θ_{FF} between 0° and 90°.

the He yield loss was lowest on port 4 the shape of the spectrum obtained from this port was used as a guide in the reconstruction of the spectra from ports 2 and 3. The resulting correction factors were then fitted as a function of θ_{BCS}. Corrections to the He yields were then obtained from the fit on a bin by bin basis at the angle corresponding to the center of each bin. These corrections ranged from 4.8% for port 4 to 16% for port 2.

When converting the double differential cross sections from the laboratory reference frame to the frame of the recoiling fissioning nucleus, the following estimates and assumptions were made:

(1) The incomplete fusion stage was assumed to be a binary reaction.

(2) Since the Bragg curve spectrometer provides no mass identification for the projectile fragment, it was assumed that each Z group detected in the Bragg curve spectrometer could be represented by a single isotope. The isotopes chosen were ^{4}He, ^{7}Li, ^{9}Be, ^{11}B, ^{12}C, ^{14}N, and ^{16}O.

(3) Wilczyński's Q_{opt} model [20] was used to estimate a representative kinetic energy for each projectile fragment group, and the corresponding excitation energy of the incomplete fusion residue (i.e., the fissioning nucleus). These quantities were used in the calculation of the kinematic transformation. The arrows in Fig. 8 show the ejectile energies predicted by the Q_{opt} model.

(4) It was assumed that there was no prefission particle emission, that all fission events were symmetric in the mass of the fission fragments, and Viola systematics [21] were used to estimate the fission fragment kinetic energies in the rest frame of the fissioning nucleus.

The first assumption is regarded as reasonably safe at the present relatively low beam energy. The consequences of the second assumption will be discussed later. The effect of the third and fourth assumptions has been tested by calculating the kinematic transformation using a range of reasonable values for the projectile fragment energy and fission fragment mass asymmetry. It was found that the estimated center-of-mass frame angles were within 3.5° of the actual angles in the worst case.

In the recoiling nucleus center-of-mass frame as it is shown in Fig. 9 [23], the angle θ is defined as the angle between the fission direction and the axis perpendicular to the plane of the incomplete fusion reaction. The angle between the projection of the fission direction onto the reaction plane and the recoil axis is defined as ϕ. Assumed symmetries about $\theta = 90°$ and $\phi = 0°$ and 90°, based on the assumption of compound nucleus decay, are used to move all of the data points into the region bounded

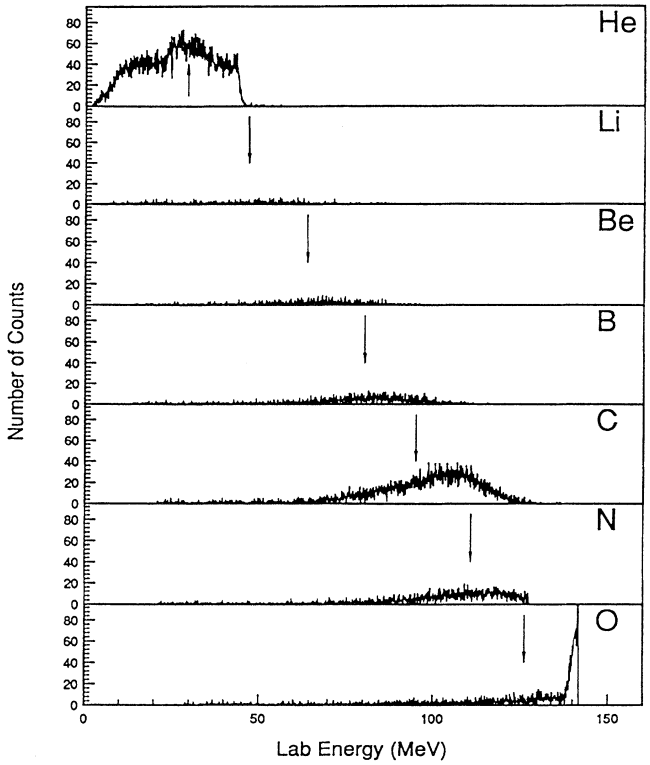

FIG. 8. Energy spectra of the incomplete fusion products in coincidence with fission fragments summed over all $\phi_{\mathrm{BCS}} = 0°$ runs on ports 2–4, and over all θ_{FF} between 0° and 90°. The He group is cut off at higher energies because the range exceeds the detector thickness. Arrows indicate the ejectile energy predicted by the Q_{opt} model. The peak near 140 MeV in the O spectrum is due to accidental coincidences between fission fragments and the very intense elastically scattered beam particles. These accidental coincidences were excluded from the coincidence yields.

by θ = 0° and 90° and ϕ = 0° and 90°. The transformation to the recoiling nucleus center-of-mass frame was performed separately for the data corresponding to each Bragg curve spectrometer position bin, using the geometric center of the bin as the assumed angle of emission of the incomplete fusion product. As an example, Fig. 10 shows the distribution of data points in θ and ϕ before and after invoking the symmetries mentioned above, for a C ejectile detected in the center bin of port 3. Each branch of the distribution corresponds to a different azimuthal angle of the Bragg curve spectrometer, while each data point corresponds to a fission fragment detector position. The validity of the assumptions of symmetry about θ = 90° and ϕ = 0° and 90° is supported by the data in Figs. 11 and 12, both of which show subsets of the angular correlation data for He and C incomplete fusion ejectiles averaged over all Bragg curve spectrometer posi-

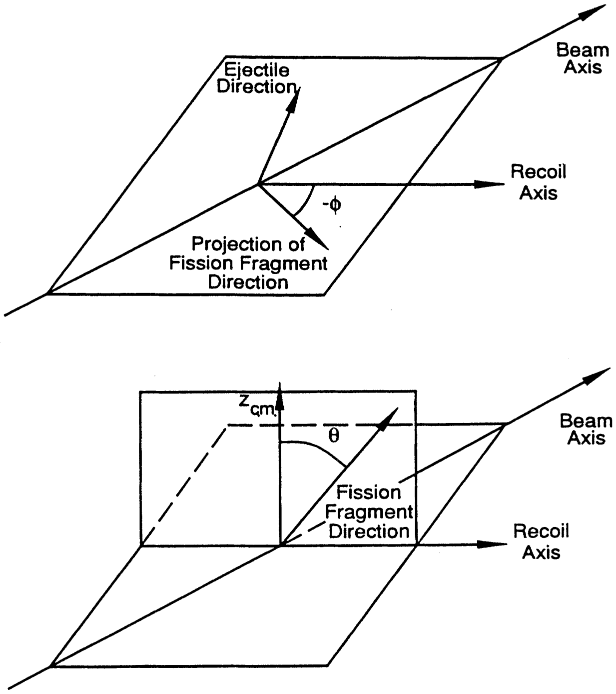

FIG. 9. Definition of θ and ϕ in the recoiling nucleus center-of-mass frame.

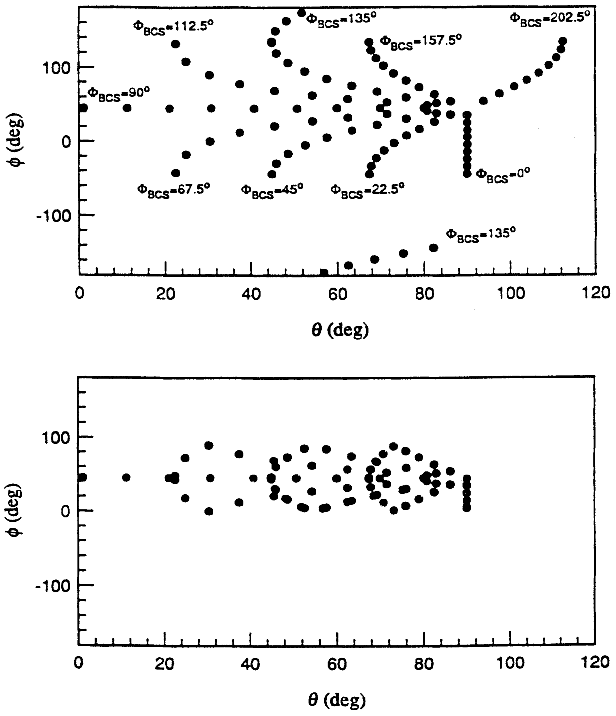

FIG. 10. Results of the coordinate transformation when C is the incomplete fusion product, corresponding to the central Bragg curve spectrometer bin in port 3, without folding and with folding about assumed lines of symmetry. When ϕ_{BCS} was set to 135°, θ_{FF} varied from 0°–170°. Otherwise θ_{FF} varied from 0°–90°.

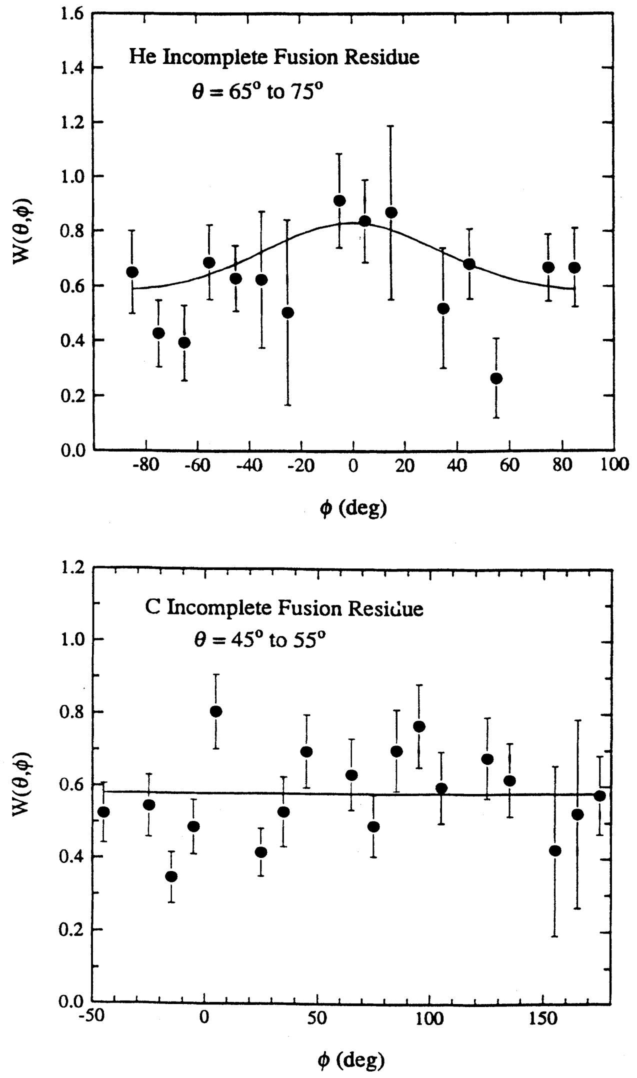

FIG. 11. Cuts through the fission fragment angular correlation data perpendicular to the θ axis, showing symmetric behavior about ϕ = 0° and 90°. The solid curves are calculations using the best fit parameters for port 3 from the fits to the angular correlations.

tion bins for port 3. Figure 11 shows cuts perpendicular to the θ axis, made before folding the data about $\phi = 0°$ and $90°$. The solid curves are calculations based on the fits to the angular correlations discussed in Sec. IV, and serve to illustrate the symmetries about $\phi = 0°$ and $90°$ expected from the theory. Figure 12 shows subsets of the data corresponding to $\phi_{\mathrm{BCS}} = 157.5°$ and $202.5°$, projected onto the θ axis before folding the data about $\theta = 90°$. As can be seen in Fig. 10, the locations of the data points for these two ϕ_{BCS} angles are mirror symmetric about $\theta = 90°$, and so the projection onto the θ axis should show symmetry about $\theta = 90°$. Although the statistical uncertainties are large, the data are fully consistent with the expected symmetries. The data of Dyer *et al.* [23] and Steckmeyer *et al.* [24] for reactions involving heavier projectiles also display the expected symmetries whenever they cross $\theta = 90°$ and $\phi = 0°$ and $90°$.

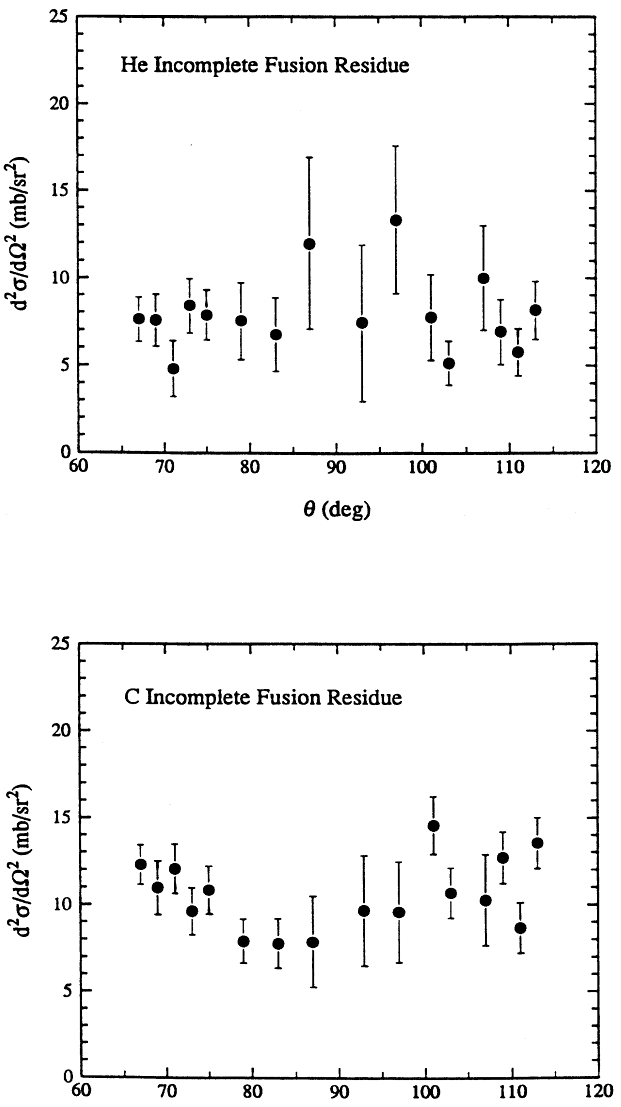

FIG. 12. Subsets of the fission fragment angular correlation data corresponding to $\phi_{\mathrm{BCS}} = 157.5°$ (below $\theta = 90°$) and $202.5°$ (above $\theta = 90°$) projected onto the θ axis. The data should be symmetric about $\theta = 90°$ (see Fig. 10).

Multiplying by $\sin\theta\,\sin\theta_{\mathrm{BCS}}$ and integrating over all θ and ϕ gives $d\sigma/d\theta_{\mathrm{BCS}}$ for a particular Bragg curve spectrometer position bin. There are seven position bins for each of the three Bragg curve spectrometer ports, so a total of 147 such integrations were performed corresponding to the 21 position bins and 7 ejectiles. To perform the integration, the θ, ϕ space was divided into 9×3 segments in θ and ϕ, respectively, and the cross sections of the data points in a segment were averaged over the entire segment. Figure 13 shows the resulting differential cross sections for all of the incomplete fusion channels as a function of the Bragg curve spectrometer position bin angles. Because the distributions have been multiplied by $\sin\theta_{\mathrm{BCS}}$ they must go to zero at 0°. Each distribution was extrapolated to zero cross section at large angles for the purpose of integrating the angular distributions to obtain the total cross section for that incomplete fusion channel.

The target thickness was measured with a low energy ^{16}O beam, while the experiment was performed using a 140 MeV ^{16}O beam. It must be assumed that the position and shape of the beam spot on the target were different for these two measurements, and so the nonuniformity of the areal density of the target across its face leads to uncertainty in the absolute cross section. The nonuniformity of the targets used here is unknown, and it was conservatively decided to adopt a value of 10% for the overall uncertainty in the absolute cross sections of the inclusive measurements reported here.

For the statistical uncertainties of the yields corresponding to the stronger incomplete fusion channels, Poisson statistics was assumed, and the statistical uncertainty of each measurement was taken as the square root of the yield. There were instances, however, in which one or more Bragg curve spectrometer position bins had no events. In the case of the He and C channels, about 20% and 17%, respectively, of the bins were empty. In the case of the Li channel, 75% of the bins were empty. In the cases where one or more bins were empty, and for uncertainty estimation purposes only, the yields of all seven position bins were added together, and the uncertainty was calculated from Poisson statistics based on the mean number of events per bin. This uncertainty was assigned to all seven position bins.

During the integration of the coincidence cross sections in θ, ϕ space, there were sometimes segments which contained no data. The Li channel was the worst case, where in some extreme cases 30% of the segments contained no data. In those cases, the value of the cross section obtained from the neighboring segment differing in ϕ was used. This approximation was deemed reasonable, given that the angular distribution anisotropy is at its minimum in the area of the sectors without any data. Mainly for this reason, an estimate of 15% was used for the uncertainty in the total cross sections obtained from the coincidence data. The error bars appearing in the angular distributions reflect the estimated statistical uncertainties only.

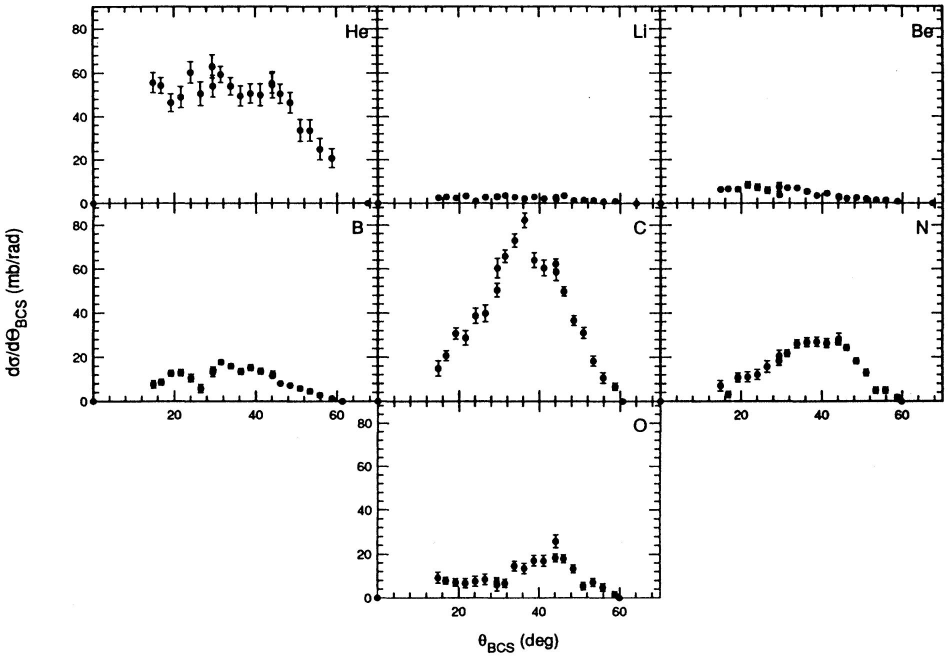

FIG. 13. $d\sigma/d\theta_{BCS}$ for all incomplete fusion channels. All graphs have the same vertical scale.

V. RESULTS

Figure 4 shows the inclusive fission fragment angular distribution in the lab frame. Figure 5 shows the same data after conversion to the center-of-mass reference frame by making the (incorrect) assumption of complete fusion followed by symmetric fission, compared with the results of Back *et al.* [17]. The present result for the total fission cross section is 1790 ± 180 mb, compared to 1655 ± 85 mb reported by Back *et al.*

The angular distributions shown in Fig. 13 correspond to the laboratory angular distributions of incomplete fusion products for events which lead to fission. By integrating the area under these angular distributions, the total cross section for incomplete fusion followed by fission is obtained for each incomplete fusion product Z. These cross sections are tabulated in Table II. The total cross section for all incomplete fusion channels (He and heavier only) combined is 747 ± 112 mb. The He cross sections have been corrected for loss of high energy particles which punch through the Bragg curve spectrometer, and also for loss of He ions which are emitted at angles greater than the 60° maximum angle of the Bragg curve spectrometer. These corrections were discussed in Sec. IV.

TABLE II. Incomplete fusion cross sections.

Ejectile	σ_{total}(mb)
He	285±43
Li	14±2
Be	29±4
B	56±8
C	220±33
N	85±13
O	58±9
Total	747±112

To obtain data which can be used for comparison with the theoretical angular distribution formula discussed in the theory section, it is necessary to start with values of the double differential cross sections in the frame of the recoiling fissioning nucleus for a given Z of the incomplete fusion product. To improve the statistical accuracy of the data, all data sets from a given Bragg curve spectrometer port (i.e., seven position bins) were averaged. Cuts were then made through the data in the θ (out-of-plane), and ϕ (in-plane) directions, to produce the coincidence angular distributions shown in Figs. 14–17. The angles cuts were approximately 15° wide.

VI. THEORY

The saddle-point transition state model (STSM) was used to fit the coincidence fission fragment angular distributions. The K distribution was predicted using the rotating liquid drop model (RLDM) using estimates of the transferred angular momentum obtained from Wilczyński's Q_{opt} model. The RLDM calculations performed here used the $\mathcal{J}_{\parallel}$ and $\mathcal{J}_{\perp}$ results of Cohen *et al.* [25]. The semiclassical angular correlation theory described by Dyer *et al.* [23] was used because it is computationally easier and agrees well with the full quantum mechanical calculation [26]. The reaction plane is defined as the plane containing the beam axis and the recoil direction of the fissioning nucleus. In the center-of-mass frame of the recoiling fissioning nucleus, the z axis is defined to be perpendicular to the reaction plane (Fig. 9). The projection of the transferred angular momentum J onto the z axis defines M. The projection of J onto the nuclear symmetry axis defines K. The polar angle θ is referenced to the z axis and the azimuthal angle ϕ is the angle between the recoil axis and the projection of the fission direction onto the reaction plane. The angle β is defined as the angle between the angular momentum direction and the nuclear symmetry axis. Since the nonrotational component of the angular momentum is expected to be small compared with J, it was assumed that $M \approx J$.

If it is assumed that J is aligned with the z axis, so that $M = J$, and the nucleus fissions along the nuclear symmetry axis, then the fission fragment angular distribution for a given J and K is given by the expression [1]:

$$W^J_{J,K}(\theta) = \left(\frac{1}{2}\right)(2J+1)|d^J_{JK}(\theta)|^2 \ . \qquad (1)$$

In the case of interest to us, i.e., incomplete fusion followed by fission, there are several mechanisms which can

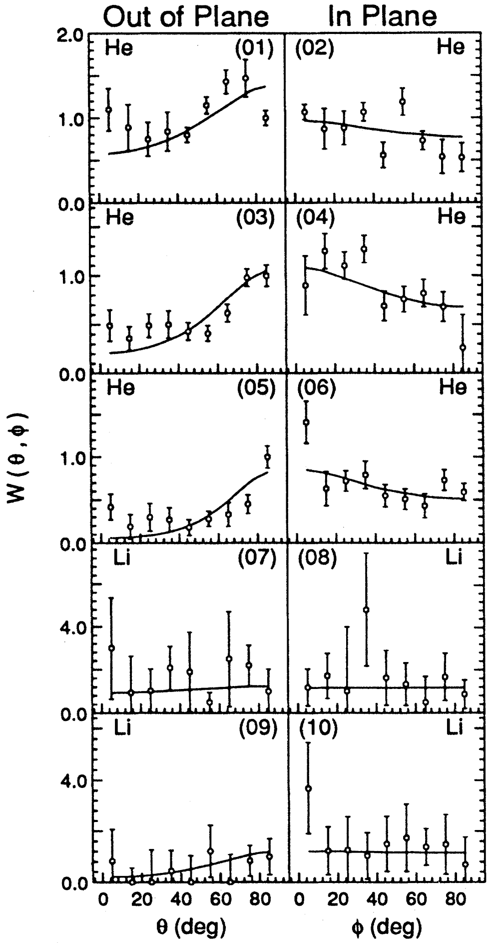

FIG. 14. Angular correlations in the reference frame of the recoiling fissioning nucleus for fission fragments in coincidence with He and Li. The solid curves are fits using the saddle-point transition state model. The numbers in parentheses refer to Table VI.

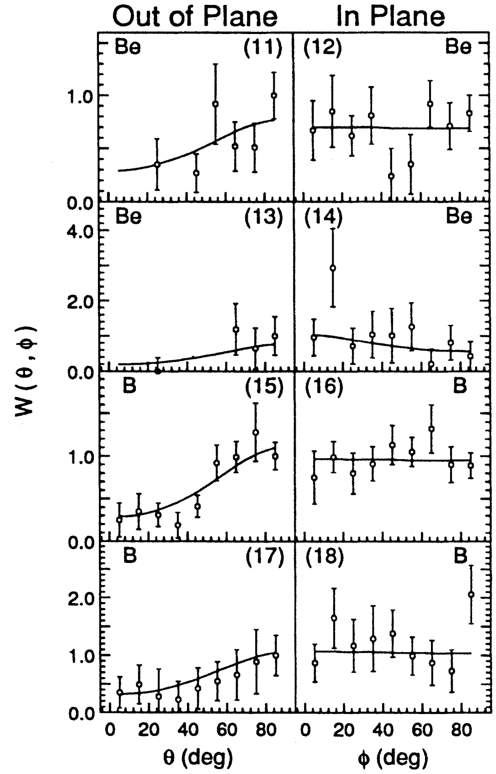

FIG. 15. Angular correlations in the reference frame of the recoiling fissioning nucleus for fission fragments in coincidence with Be and B. The solid curves are fits using the saddle-point transition state model. The numbers in parentheses refer to Table VII.

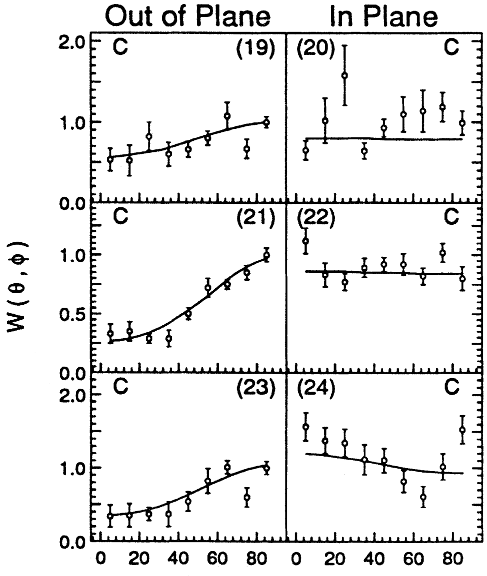

FIG. 16. Angular correlations in the reference frame of the recoiling fissioning nucleus for fission fragments in coincidence with C. The solid curves are fits using the saddle-point transition state model. The numbers in parentheses refer to Table VIII.

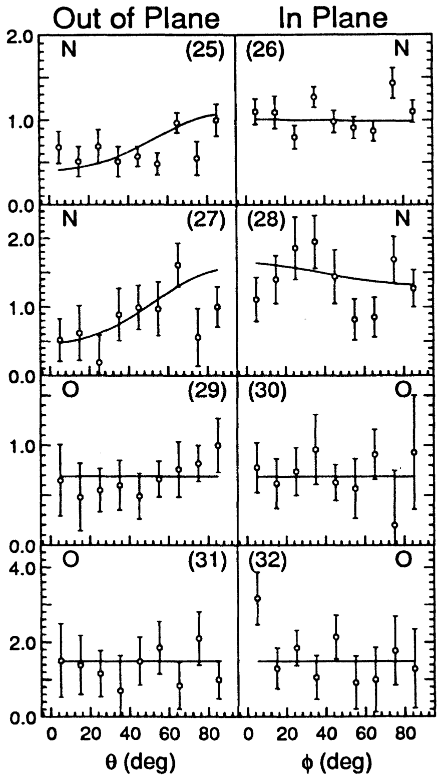

FIG. 17. Angular correlations in the reference frame of the recoiling fission nucleus for fission fragments in coincidence with N and O. The solid curves are fits using the saddle-point transition state model. The numbers in parentheses refer to Table IX.

cause J not to be perfectly normal to the reaction plane [23]. The effect on the angular distribution of components having $M \neq J$ is simulated by weighting it with a distribution in the angle α [23], where α is the angle between J and the z axis. It is assumed that J lies in a plane perpendicular to the direction of the recoiling fissioning nucleus [23,26]. The angle β between J and the symmetry axis is given by

$$\beta = \cos^{-1}(\cos\theta\cos\alpha + \sin\theta\sin\alpha\sin\phi) \ . \tag{2}$$

The probability that the nuclear symmetry axis is at an angle β with respect to the J vector is taken as

$$W^J_{J,K}(\theta,\phi) = \left(\frac{1}{2}\right)(2J+1)|d^J_{JK}(\beta)|^2 \ . \tag{3}$$

Equation (3) gives the angular distribution for a given combination of J and K. The weighting factor associated with the distribution of the angular momentum J is given by

$$P(J) \propto \sum_J \rho(J)(2J+1) \ , \tag{4}$$

where ρ is the strength with which each J is populated. The weighting factor associated with the K distribution is given by

$$P(K) \propto \left[\sum_{-J}^{J} \exp(-K^2/2K_0^2)\right]^{-1} \exp(-K^2/2K_0^2) \ . \tag{5}$$

The width K_0 of the K distribution will be discussed in detail below. The weighting factor used for the α distribution is assumed to be Gaussian with width α_0:

$$P(\alpha) \propto \int_{-\pi}^{\pi} e^{\left(\frac{-\alpha^2}{2\alpha_0{}^2}\right)} d\alpha \ . \tag{6}$$

The final expression for the fission fragment angular distribution is [23]

$$W(\theta,\phi) \sim \sum_J \rho(J)(2J+1) \times \sum_{K=-J}^{J} e^{\left(\frac{-K^2}{2K_0{}^2}\right)} \times \int_{-\pi}^{\pi} e^{\left(\frac{-\alpha^2}{2\alpha_0{}^2}\right)} |d^J_{JK}(\beta)|^2 d\alpha \ , \tag{7}$$

where the quantity d^J_{JK} is the Wigner D function with the general form

$$d^J_{MK}(\beta) = \sqrt{(J+M)!(J-M)!(J+K)!(J-K)!}\sum_k (-1)^k \frac{\left(\cos\frac{\beta}{2}\right)^{2J-2k+M-K}\left(\sin\frac{\beta}{2}\right)^{2k-M+K}}{k!(J+M-k)!(J-K-k)!(K-M+k)!} \ . \tag{8}$$

It has been observed that the form of the J distribution has a negligible effect on the fission fragment angular distribution shape [27,19]. It is the average value of the transferred angular momentum that is important. Hence a simplified form for the spin distribution can be used:

$$\rho(J) = \delta(J - J_0) \ . \tag{9}$$

This simplification reduces the summation over J to the single term $(2J_0 + 1)$.

The K distribution is determined by the K dependence of the level density at the saddle point, and it can be given in a Gaussian form [23] with width K_0. The quantity K_0 can be written in terms of the effective moment of inertia and the nuclear temperature, T, at the saddle point [28]:

$$K_0^2(J) = \frac{\mathcal{J}_{\rm sph}}{\hbar^2}\frac{T}{\mathcal{J}_{\rm sph}/\mathcal{J}_{\rm eff}(J)} \ . \tag{10}$$

The quantities $\mathcal{J}_{\|}(I)/\mathcal{J}_{\rm sph}$ and $\mathcal{J}_{\perp}(J)/\mathcal{J}_{\rm sph}$ for each incomplete fusion channel were obtained from published curves calculated using the liquid drop model [25]. Since the intrinsic spins of the interacting nuclei are neglected, one can use $J \approx l$, where l is the orbital angular momentum in the entrance channel. The nuclear temperature of the fissioning nucleus, which depends on the intrinsic energy per nucleon, is given in an approximate spin independent form by [28]

$$T = \sqrt{\left(\frac{8}{A}\right)\left(E_{\mathrm{c.m.}} + Q - \langle E_{\mathrm{rot}} \rangle - E_{\mathrm{pp}}\right)}\ , \qquad (11)$$

where E_{cm} is the energy in the frame of the recoiling nucleus of the *transferred mass*, Q is the Q value of the reaction in which the mass is transferred, $\langle E_{\mathrm{rot}} \rangle = \hbar^2 \langle J^2 \rangle / 2\mathcal{J}_{\mathrm{sph}}$ is the rotational energy of the fissioning nucleus, and E_{pp} is the energy removed by any prefission particle emission (taken to be zero here). Wilczyński's Q_{opt} model [20] was used to estimate the transferred angular momentum J. The transferred angular momenta are calculated assuming an interaction distance in the entrance channel which corresponds to the sum of the half-density radii. The interaction distance of the final channel was calculated taking into account recoil effects during the nucleon transfer [29].

The values of the transferred angular momenta were calculated corresponding to the minimum, Q_{opt} and grazing conditions for each incomplete fusion channel. The transferred angular momenta corresponding to the limiting and grazing cases are considered to span the range of plausible angular momentum transfers. The values of K_0 corresponding to these J values were calculated using the liquid drop model (see Fig. 11 of Cohen *et al.* [25]). It was found that K_0 is not sensitive to J over the range of J values considered for the incomplete fusion channels studied here.

Having calculated K_0 from the liquid drop model for the J values corresponding to the optimum Q value, the angular distribution expression (7) with condition (9) was fitted to the measured angular correlations for all of the ejectiles except O. In the case of O the data are compared with the results of Eq. (7) for $J = 0$. During these fits K_0 was held constant while J and α_0 were treated as free parameters. As a check that the K_0 values are sufficiently insensitive to J, the best fit values of J were used to determine K_0 once more from the liquid drop model, and the data were fitted again to determine the optimum values of J and α_0 for the new K_0 values. It was found in the case of the He channel (the worst case), that the value of K_0 that resulted from the first iteration was within 2% of the starting K_0 value, and subsequent iterations showed no change. For all incomplete fusion channels the fissioning nucleus was predicted to be strongly deformed at the saddle point, so that the STSM should be valid for these cases. The fits are shown in Figs. 14–17, and the results are summarized in Tables III to V. The J, α_0, K_0, and χ^2 per degree of freedom corresponding to each incomplete fusion channel are given for ports 3 and 4. On port 2, only the He and C channels had good enough statistics to be worth fitting. For each incomplete fusion channel the parameters are fitted simultaneously to cuts in the in-plane and the out-of-plane direction. The column labeled θ_{avg} shows the average value of θ for the in-plane cut, ϕ_{avg} shows the average value of ϕ for the out-of-plane cut. Tables VI to IX show the fitted parameters.

TABLE III. θ_{avg}, ϕ_{avg}, $J_{Q_{\mathrm{opt}}}$, J, α_0, K_0, and χ^2 for port No. 2.

Ejectile	θ_{avg}	ϕ_{avg}	$J_{Q_{\mathrm{opt}}}$	J	α_0	K_0	χ^2
He	45.0°	45.0°	42	57±45	55 ± 14	16.758	3.1
C	50.0°	22.5°	12	12±2	3±7	10.733	2.0

TABLE IV. θ_{avg}, ϕ_{avg}, $J_{Q_{\mathrm{opt}}}$, J, α_0, K_0, and χ^2 for port No. 3.

Ejectile	θ_{avg}	ϕ_{avg}	$J_{Q_{\mathrm{opt}}}$	J	α_0	K_0	χ^2
He	87.5°	10.0°	42	39±4	34±6	16.758	2.0
Li	65.0°	22.5°	30	11±9	6±10	13.930	0.6
Be	70.0°	37.5°	23	18±6	2±14	12.413	2.2
B	70.0°	37.5°	16	19±2	2±12	11.141	0.7
C	70.0°	45.0°	12	18±1	3±9	10.733	1.6
N	72.5°	52.5°	6	12±2	5±14	8.243	2.2
O	70.0°	60.0°	0	-	-	7.648	0.5

Figure 18 shows the transferred angular momenta (averaged over all ports) determined from the fits to the data compared with the transferred angular momentum predicted by the Q_{opt} model, as a function of the number of captured nucleons. The vertical error bars on the observed transferred angular momentum represent the uncertainties in the fitted J values. The assumption made here that the observed incomplete fusion Z groups can be represented by a single transferred mass is arbitrary. To investigate the effect of this assumption on the fitted J values, the angular correlation data for N and C were converted to the center of mass and fitted again, assuming several different values for the transferred mass. It was found that the values of the transferred angular momenta extracted from the data are essentially the same for N if the transferred mass is assumed to be 1, 2, or 3 nucleons, and essentially the same for C if the transferred mass is assumed to be 2, 3, or 4 nucleons. Thus the effect on the transferred angular momenta extracted from the data if the assumed number of transferred nucleons is wrong is to move them horizontally. The horizontal bars on the fitted angular momenta show the effect if the assumed mass transfer is wrong by ±1 unit. The values of the transferred angular momentum predicted by the Q_{opt} model were sensitive only to the number of transferred nucleons (i.e., the Z of the outgoing projectile fragment does not matter, only the mass does).

Figure 18 shows that the transferred angular momenta

TABLE V. θ_{avg}, ϕ_{avg}, J, $J_{Q_{\mathrm{opt}}}$, α_0, K_0, and χ^2 for port No. 4.

Ejectile	θ_{avg}	ϕ_{avg}	$J_{Q_{\mathrm{opt}}}$	J	α_0	K_0	χ^2
He	87.5°	10.0°	42	49±7	29±5	16.758	1.9
Li	87.5°	22.5°	30	27±13	2±10	13.930	0.2
Be	87.5°	37.5°	23	32±6	40±16	12.413	1.0
B	87.5°	37.5°	16	18±4	4±17	11.141	0.6
C	87.5°	45.0°	12	20±2	29±5	10.733	2.5
N	72.5°	52.5°	6	16±3	28±12	8.243	1.6
O	87.5°	60.0°	0	-	-	7.648	0.8

TABLE VI. Details of the fits to the He and Li data.

Figure	Graph	Ejectile	Port No.	θ	ϕ	K_0	α_0	J
14	1	He	2	0°–90°	45.0°	16.758	55°	57
14	2	He	2	45.0°	0°–90°	16.758	55°	57
14	3	He	3	0°–90°	10.0°	16.758	34°	39
14	4	He	3	87.5°	0°–90°	16.758	34°	39
14	5	He	4	0°–90°	10.0°	16.758	29°	49
14	6	He	4	87.5°	0°–90°	16.758	29°	49
14	7	Li	3	0°–90°	22.5°	13.930	6°	11
14	8	Li	3	65.0°	0°–90°	13.930	6°	11
14	9	Li	4	0°–90°	22.5°	13.930	2°	27
14	10	Li	4	87.5°	0°–90°	13.930	2°	27

TABLE VII. Details of the fits to the Be and B data.

Figure	Graph	Ejectile	Port No.	θ	ϕ	K_0	α_0	J
15	11	Be	3	0°–90°	37.5°	12.413	2°	18
15	12	Be	3	70.0°	0°–90°	12.413	2°	18
15	13	Be	4	0°–90°	37.5°	12.413	40°	32
15	14	Be	4	87.5°	0°–90°	12.413	40°	32
15	15	B	3	0°–90°	37.5°	11.141	2°	19
15	16	B	3	70.0°	0°–90°	11.141	2°	19
15	17	B	4	0°–90°	37.5°	11.141	4°	18
15	18	B	4	87.5°	0°–90°	11.141	4°	18

TABLE VIII. Details of the fits to the C data.

Figure	Graph	Ejectile	Port No.	θ	ϕ	K_0	α_0	J
16	19	C	2	0°–90°	22.5°	10.733	3°	12
16	20	C	2	50.0°	0°–90°	10.733	3°	12
16	21	C	3	0°–90°	45.0°	10.733	3°	18
16	22	C	3	70.0°	0°–90°	10.733	3°	18
16	23	C	4	0°–90°	45.0°	10.733	29°	20
16	24	C	4	87.5°	0°–90°	10.733	29°	20

TABLE IX. Details of the fits to the N and O data.

Figure	Graph	Ejectile	Port No.	θ	ϕ	K_0	α_0	J
17	25	N	3	0°–90°	52.5°	8.243	5°	12
17	26	N	3	72.5°	0°–90°	8.243	5°	12
17	27	N	4	0°–90°	52.5°	8.243	28°	16
17	28	N	4	72.5°	0°–90°	8.243	28°	16
17	29	O	3	0°–90°	60.0°	7.648	-	0
17	30	O	3	70.0°	0°–90°	7.648	-	0
17	31	O	4	0°–90°	60.0°	7.648	-	0
17	32	O	4	87.5°	0°–90°	7.648	-	0

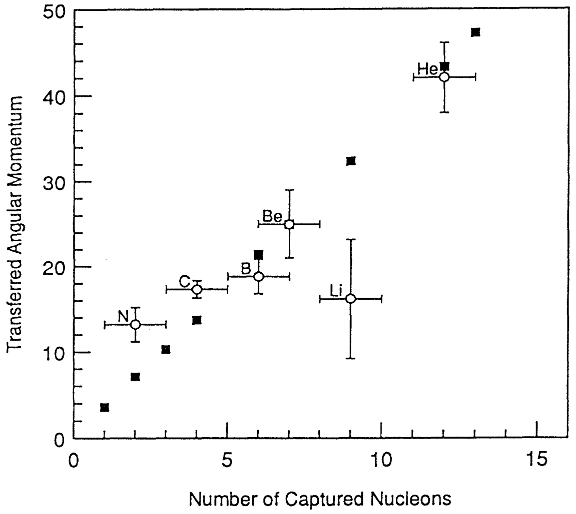

FIG. 18. Transferred angular momentum versus number of captured nucleons. Filled squares indicate the transferred angular momentum values predicted by the $Q_{\rm opt}$ model, open circles represent the values obtained by fitting the data. The uncertainty in the horizontal direction shows the effect if the transferred mass differs from the assumed one by ± one nucleon. The labels adjacent to the experimental data points indicate the Z of the incomplete fusion product.

predicted by the $Q_{\rm opt}$ model are in good agreement with our observations except for the small mass transfers. This may be a consequence of the fact that the $Q_{\rm opt}$ model assumes an interaction distance in the entrance channel corresponding to the sum of the half-density radii. Thus all incomplete fusion reactions are assumed to occur at the same impact parameter, regardless of the transferred mass. This is not necessarily correct. Wilczyński's "Sum Rule Model" [20], for example, predicts that smaller mass transfers will occur at larger impact parameters. If the smaller mass transfers are assumed to occur at larger impact parameters, the $Q_{\rm opt}$ model predicts larger transferred angular momenta.

VII. SUMMARY AND CONCLUSIONS

This paper presents the results of measurements for the reaction ^{16}O+^{232}Th at 140 MeV of total cross sections for the incomplete fusion channels in coincidence with fission fragments. An inclusive angular distribution was measured, and the total fission cross section, 1790±180 mb, was in excellent agreement with a previously reported measurement [17]. The percentage of the total cross section due to incomplete fusion, including only He and heavier incomplete fusion products, was approximately 42%. The major contributions to the incomplete fusion channels were from the C and He incomplete fusion channels.

Wilczyński's $Q_{\rm opt}$ model was used to estimate kinematic quantities needed to transform the coincidence data from the lab to the center-of-mass reference frame of the recoiling fissioning nucleus. It was also used to estimate the angular momentum transfer in the incomplete fusion reactions. These estimates of the transferred angular momentum were used to obtain predicted K_0 values from the rotating liquid drop model, which in turn were used in the analysis of the measured angular correlation data. The predicted K_0 values were insensitive to the values used for the transferred angular momenta. The values of K_0 found for all of the incomplete fusion channels indicated that the fissioning nucleus is quite deformed at the saddle point, so the STSM should be valid.

Angular correlation data were obtained by making inplane and out-of-plane cuts through the measured coincidence cross sections in the center-of-mass frame of the recoiling fissioning nucleus. These were fitted using the STSM with the width of the K distribution, K_0, fixed at the values obtained from the liquid drop model. The transferred angular momentum J and the width α_0 of the distribution of J around the perpendicular to the reaction plane were used as free parameters in the fits. The best fit values of J were in reasonable agreement with the estimates of the transferred angular momenta from the $Q_{\rm opt}$ model, but tend to be larger than predicted for the smallest mass transfers. This could be a consequence of the assumption in the $Q_{\rm opt}$ model that all incomplete fusion reactions occur at the same impact parameter in the entrance channel.

ACKNOWLEDGMENTS

The authors wish to acknowledge many fruitful discussions with Professor D. Robson, Profesor K. Kemper, and Profesor S. Tabor. This work was supported in part by the National Science Foundation and the state of Florida.

[1] R. Vandenbosch and J. R. Huizenga, *Nuclear Fission* (Academic Press, New York, 1973).
[2] P. David, T. Mayer-Kuckuk, and A. van der Woude, *Dynamics of Nuclear Fission and Related Collective Phenomena* (Springer-Verlag, Berlin, 1982).
[3] W. Schröder, *Nuclear Fission and Heavy-Ion-Induced Reactions* (Harwood Academic Publishers, New York, 1973).
[4] L. C. Vaz and J. M. Alexander, Phys. Rep. **97**, 1 (1983).
[5] R. Freifelder, M. Prakash, and J. M. Alexander, Phys. Rep. **133**, 315 (1986).
[6] A. Bohr, *Proceedings of the International Conference on the Peaceful Uses of Atomic Energy*, Geneva, 1955 (United Nations, New York, 1956), Vol. 2, p. 131.
[7] B. B. Back, H. C. Clerc, R. R. Betts, B. G. Glagola, and B. D. Wilkins, Phys. Rev. Lett. **46**, 1068 (1981).
[8] B. B. Back, R. R. Betts, K. Cassidy, B. G. Glagola, J. E. Gindler, L. E. Glendenin, and B. D. Wilkins, Phys. Rev.

Lett. **50**, 818 (1983).

[9] K. T. Lesko, S. Gil, A. Lazzarini, V. Metag, A. G. Seamster, and R. Vandenbosch, Phys. Rev. C **27**, 2999 (1983).

[10] V. S. Ramamurthy and S. S. Kapoor, Phys. Rev. Lett. **54**, 178 (1985).

[11] V. S. Ramamurthy and S. S. Kapoor, Phys. Rev. C **32**, 2182 (1985).

[12] B. B. Back, Phys. Rev. C **31**, 2104 (1985).

[13] P. D. Bond, Phys. Rev. C **32**, 471 (1985).

[14] P. D. Bond, Phys. Rev. C **32**, 483 (1985).

[15] H. Rossner, J. R. Huizenga, and W. U. Schröder, Phys. Rev. Lett. **53**, 38 (1984).

[16] H. Rossner, J. R. Huizenga, and W. U. Schröder, Phys. Rev. C **33**, 560 (1986).

[17] B. B. Back, R. R. Betts, J. E. Gindler, B. D. Wilkins, and S. Saini, Phys. Rev. C **32**, 195 (1985).

[18] J. P. Lestone, J. R. Leigh, J. O. Newton, and J. X. Wei, Nucl. Phys. **A509**, 178 (1990).

[19] F. Videbaek, S. G. Steadman, G. G. Batrouni, and J. Karp, Phys. Rev. C **35**, 2333 (1987).

[20] J. Wilczyński, K. Siwek-Wilczyńska, J. van Driel, S. Gonggrijp, D. C. J. M. Hageman, R. V. F. Janssens, J. Łukasiak, R. H. Siemssen, and S. Y. van der Werf, Nucl. Phys. **A373**, 109 (1982).

[21] V. E. Viola, K. Kwiatkowski, and M. Walker, Phys. Rev. C **31**, 1550 (1985).

[22] A. D. Frawley, L. H. Wright, R. C. Kline, E. P. Gavathas, and L. C. Dennis, Nucl. Instrum. Methods Phys. Res. A **306**, 512 (1991).

[23] P. Dyer, R. J. Puigh, R. Vandenbosch, T. D. Thomas, M. S. Zisman, and L. Nunnelley, Nucl. Phys. **A322**, 205 (1979).

[24] J. C. Steckmeyer, F. Lefebvres, C. Le brun, J. F. Lecolley, M. L'Haridon, A. Osmont, and J. P. Patry, Nucl. Phys. **A427**, 357 (1984).

[25] S. Cohen, F. Plasil, and W. J. Swiatecki, Ann. Phys. (N.Y.) **82**, 577 (1974).

[26] B. B. Back and S. Bjørnholm, Nucl. Phys. **A302**, 343 (1978).

[27] P. Dyer, R. J. Puigh, R. Vandenbosch, T. D. Thomas, and M. S. Zisman, Phys. Rev. Lett. **39**, 392 (1977).

[28] H. Rossner, D. Hilscher, E. Holub, G. Ingold, U. Jahnke, H. Orf, J. R. Huizenga, J. R. Birkelund, W. U. Schröder, and W. W. Wilcke, Phys. Rev. C **27**, 2666 (1983).

[29] R. Bass, *Nuclear Reactions with Heavy Ions* (Springer-Verlag, Berlin, 1980).